PHOTONICS

10.1126/sciadv.1600149

Domain morphology, boundaries, and topological defects in biophotonic gyroid nanostructures of butterfly wing scales

Andrej Singer,[1]* Leandra Boucheron,[1] Sebastian H. Dietze,[1] Katharine E. Jensen,[2] David Vine,[3] Ian McNulty,[4] Eric R. Dufresne,[2] Richard O. Prum,[2] Simon G. J. Mochrie,[2] Oleg G. Shpyrko[1]

Many organisms in nature have evolved sophisticated cellular mechanisms to produce photonic nanostructures and, in recent years, diverse crystalline symmetries have been identified and related to macroscopic optical properties. However, because we know little about the distributions of domain sizes, the orientations of photonic crystals, and the nature of defects in these structures, we are unable to make the connection between the nanostructure and its development and functionality. We report on nondestructive studies of the morphology of chitinous photonic crystals in butterfly wing scales. Using spatially and angularly resolved x-ray diffraction, we find that the domains are highly oriented with respect to the whole scale, indicating growth from scale boundaries. X-ray coherent diffractive imaging reveals two types of crystalline domain interfaces: abrupt changes between domains emerging from distinct nucleation sites and smooth transitions with edge dislocations presumably resulting from internal stresses during nanostructure development. Our study of the scale structure reveals new aspects of photonic crystal growth in butterfly wings and shows their similarity to block copolymer materials. It opens new avenues to exploration of fundamental processes underlying the growth of biological photonic nanostructures in a variety of species.

INTRODUCTION

Light interference, as was realized as early as the beginning of the 19th century (*1*), is a common cause of the bright coloring of various animals such as the spine of the sea mouse (*2*), butterfly wings (*3*–*7*), feathers of birds of paradise (*8*, *9*), or the skin of chameleons (*10*). The appearance ranges from narrowband colors corresponding to well-ordered nanostructures to broadband sparkly reflectance due to Anderson localization of light in strongly disordered natural photonic crystals (*11*, *12*). The remarkably diverse engineering of photonic crystals in animals and plants has practical applications such as mating and camouflage. These photonic crystals are not only interesting for evolutionary biology (*13*) but also appealing for metamaterial research (*14*–*18*) and exciting applications such as designing Weyl points (*19*). Recently, photonic crystal synthesis from butterfly wings has been successfully demonstrated by replacing the chitinous material with various metals to achieve tunable photonic properties (*20*, *21*). However, the initial growth of these photonic crystals in nature is yet to be understood, and once the self-assembly process can be duplicated in the laboratory, the new synthesis pathway will undoubtedly open up new opportunities for developing photonic devices with desired mechanical, structural, and photonic properties.

The nanoscale structure of biological photonic crystals has been studied using electron microscopy (*7*, *22*, *23*), typically by slicing techniques. The crystallographic space group symmetry of various butterfly and beetle species has recently been characterized using x-ray diffraction (*7*, *24*). Furthermore, the orientation of the photonic crystals can be visualized and mapped using optical light and cross-polarizers (*8*, *25*). Present understanding suggests that a butterfly wing scale is a thin object (about 10 μm in thickness and 100 μm in size) and forms from a single cell (*26*). The interior of the scale contains photonic microcrystals (reflectors) that are somewhat randomly oriented and consist of chitin, which slowly polymerizes in the larval stage of the butterfly after the formation of the outermost layer of the scale (*7*, *26*, *27*). The naked eye typically cannot resolve individual microcrystals, and the observer sees reflection for a range of wavelengths (pointillism) (*28*, *29*). Whether the chirality of the gyroid crystals observed in some species is connected to the molecular chirality of chitin is currently being debated (*23*). Recently, by comparing two-dimensional transmission electron micrograph sections of the green gyroid scales of *Parides sesostris* to computer models of a single-network gyroid, Yoshioka *et al.* (*25*) found that domains were not randomly oriented but preferentially oriented with the [110] direction normal to the top (or obverse) surface of the scale.

EXPERIMENT

We used x-ray diffraction to investigate the spatial and angular distributions of the photonic crystals in a single wing scale of a Kaiser-i-Hind butterfly, *Teinopalpus imperialis* (Papilionidae) (see Fig. 1A). The green upper wing scales of male species containing multiple domains of single-network gyroids ($I4_132$) (*7*, *30*) were investigated. By quantitative analysis of the orientation of photonic crystals in the entire scale, we find that the gyroid domains are preferentially oriented with the [111] direction perpendicular to the scale boundary, as opposed to the [110] direction observed in *P. sesostris* (Papilionidae) (*25*). Additionally, we used a coherent x-ray diffractive imaging technique [ptychography (*31*)] to reveal and document two qualitatively different types of gyroid domain boundaries: first, abrupt interfaces at the boundaries of domains with distinctive orientations that merge during growth, and second, boundaries with edge dislocations between subregions of a single-crystal domain with very slight variations in orientation. We anticipate that these observations will shed new light on the structural mechanisms of self-assembly (*32*) and the development of photonic structures in butterfly wing scales.

[1]University of California, San Diego, La Jolla, CA 92093, USA. [2]Yale University, New Haven, CT 06511, USA. [3]Advanced Photon Source, Argonne National Laboratory, Argonne, IL 60439, USA. [4]Center for Nanoscale Materials, Argonne National Laboratory, Argonne, IL 60439, USA.
*Corresponding author. Email: ansinger@ucsd.edu

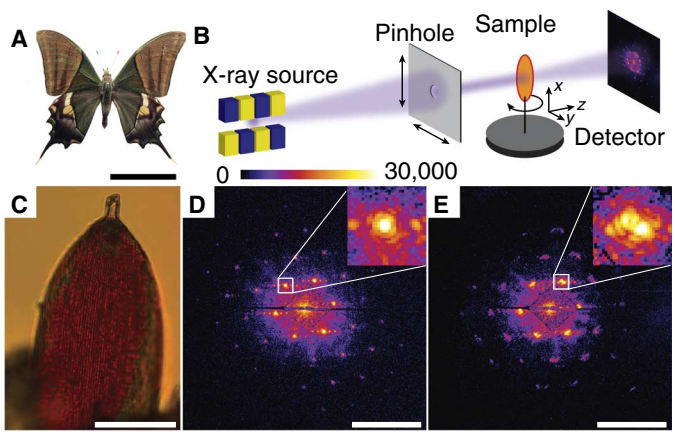

Fig. 1. Experimental description. (**A**) An image of the *T. imperialis* (Kaiser-i-Hind) butterfly (*43*). (**B**) A schematic of the experiment. X-ray radiation (1.8-keV photon energy) is generated by the undulator source and spatially filtered by a 5-μm pinhole. The sample is positioned behind the pinhole, and the detector records coherently scattered radiation. A semitransparent beam stop mounted on a metallic wire was used. (**C**) An optical micrograph of a single wing scale. (**D** and **E**) Typical diffraction patterns recorded from different sample areas with x-rays incident normal to the scale. Insets to (D) and (E) show the intensity in the vicinity of the (110) Bragg peaks. Scale bars, 5 cm (A), 50 μm (C), and 0.05 nm^{-1} (D and E).

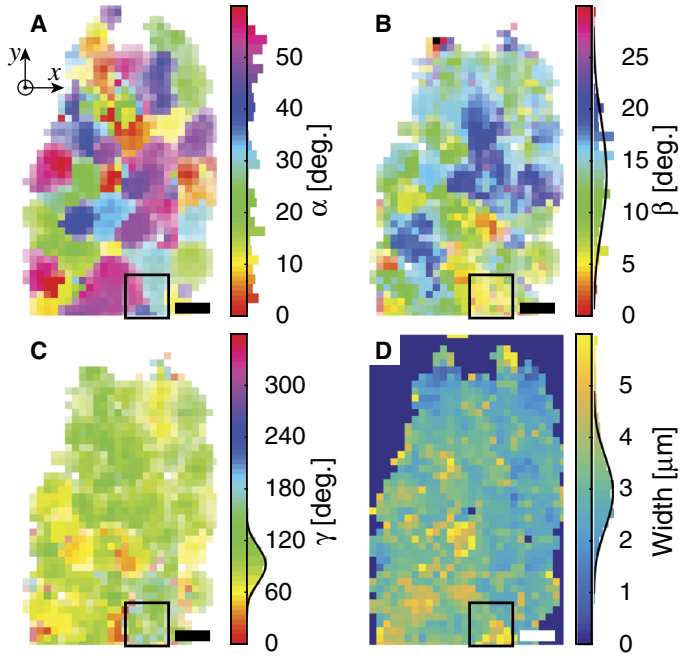

Fig. 2. A representation of the whole scale oriented similarly to Fig. 1C. (**A**) The angle α between the *x* axis and a {110} peak (see Fig. 1D) as a function of the position across the scale. An average over all six angles (modulo 60°) is shown. (**B**) The angle β between the *z* axis (out of plane of the image) and vector $\mathbf{n}_{111}$ normal to the determined hexagonal set of peaks. (**C**) The angle γ between the *x* axis and the projection of $\mathbf{n}_{111}$ onto the *xy* plane. (**D**) The thickness of the crystallites determined from the x-ray diffraction data recorded by rocking the scale through the beam. Scale bar, 10 μm; the region for the ptychographic scan is indicated by the black square and the histograms of the angles are shown on the right of the color bars. In (B) to (D), Gaussian fits to the histograms are also shown with centers (RMS widths) of 14° ± 1° (5° ± 1°) (B), 91° ± 1° (20° ± 1°) (C), and 3.0 ± 0.1 μm (0.7 ± 0.1 μm) (D). Angles are positive for clockwise rotation.

The experimental setup is shown in Fig. 1B. Coherent x-rays were spatially filtered by a pinhole and were incident on an isolated, free-standing butterfly wing scale (see Fig. 1C for an optical micrograph of the scale and Materials and Methods for details). Strong Bragg peaks reveal a highly ordered sample, and a pattern of hexagonally symmetric peaks indicates a gyroid lattice with a lattice spacing of 330 nm in the ⟨110⟩ direction, in agreement with the literature (*7*). In contrast to typical x-ray diffraction on atomic crystals, here, because of the large unit cell dimensions, the Ewald sphere is almost flat, and several reflections can be recorded simultaneously (*33*). In Fig. 1D, one set of hexagonal peaks is observed and suggests scattering from a single domain. Four orders of peaks can clearly be seen, with a maximum recorded spatial frequency corresponding to less than 60 nm. The intensity close to a {110} Bragg peak (inset to Fig. 1D) is reminiscent of an Airy pattern due to circular pinhole diffraction, indicating that the sample is a homogeneous single crystal within the pinhole area. By contrast, in Fig. 1E, two hexagonal sets of peaks with slightly different orientations are observed, indicating two domains in the illuminated region. Moreover, the diffracted intensity around the Bragg peak lacks circular symmetry because of domain boundaries in the beam (inset to Fig. 1E). The peak on the top left of the inset to Fig. 1E appears to have a minimum intensity in its center, which is a clear indicator of the presence of an edge dislocation within the illuminated volume of the sample. In both diffraction patterns, horizontal fringes around the Bragg peak reveal an additional periodicity on top of the gyroid lattice, which we ascribe to the vertical ridges, visible in Fig. 1C.

We mapped crystallographic orientations within the scale by scanning the pinhole across the sample with a step size of 2 μm for different angles of incidence ranging from −20° to +20° about the normal of the scale. These scans were used to determine the complete spatially resolved orientation (three angles) of the gyroid reciprocal lattice (see Materials and Methods and figs. S1 and S2). The orientation of the grains may be presented with the following three angles: α is the angle between the *x* axis and a {110} peak (see Fig. 1, D and E), β is the angle between the *z* axis and the normal to the plane defined by the hexagonal peaks $\mathbf{n}_{111}$, and γ is the angle between the *x* axis and the projection of the normal vector $\mathbf{n}_{111}$ along the *z* axis (see fig. S3 for the definition of the angles).

RESULTS

As expected, the scale consists of different domains revealed by the angle α (modulo 60°) presented in Fig. 2A. The histogram of angles α appears to be random, suggesting that there is no preferred orientation of the gyroid lattice within the plane of the scale. The missing signal in the uppermost part of the scale corresponds to noncrystalline material in the stem of the scale (see Fig. 1C). There is also no particular structure in the distribution of boundary angles (see fig. S4), suggesting independent growth of individual domains. We found preferred orientation in both β and γ: β = 14 ± 5 and γ = 91 ± 20. Although the orientation of the gyroid lattice is random within the plane of the scale, its normal is highly oriented. The scale was tilted along the beam

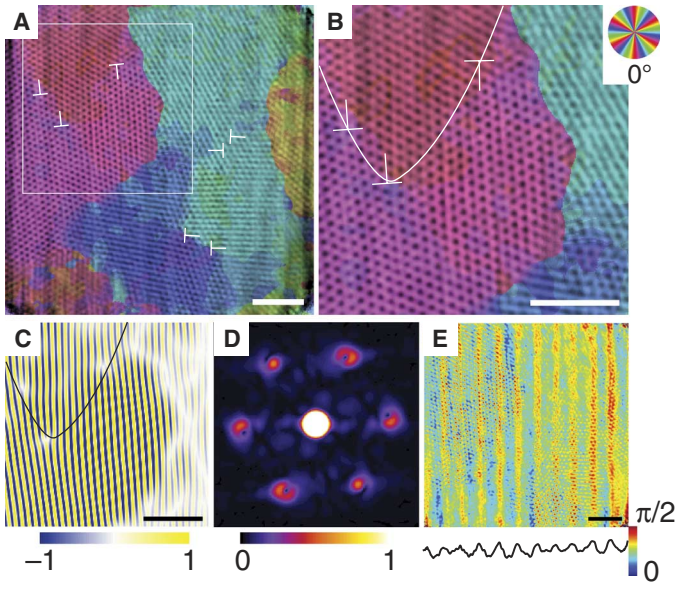

Fig. 3. Result from ptychographic reconstruction. (**A**) An image of the scale indicated by a black rectangle in Fig. 2 (absorption or reconstructed amplitudes). The color corresponds to the crystal orientation modulo 60° (see color wheel), and edge dislocations are indicated. (**B**) Zoomed-in image of the region indicated by the white square in (A). The solid line highlights the domain boundary accommodated by edge dislocations between the red (average angle, 52° ± 2°) and the dark red (average angle, 57° ± 3°) domains. (**C**) Bragg filtered image of (B) obtained by placing a mask in the Fourier transform (*35*). (**D**) Squared modulus of a Fourier transform of the sample transmission function (B) multiplied by a Gaussian mask (0.5-μm wide) centered in the lowest indicated dislocation in (B). (**E**) Reconstructed phases. Average along the vertical is shown together with the color bar on the bottom. Scale bars, 2 μm (A to C and E).

by about 18° during the experiment, consistent with the observation that the [111] gyroid peak is perpendicular to the whole scale.

Because of the limited thickness of the crystals perpendicular to the scale, Bragg peaks are broadened along the q_z direction (see Fig. 1D). By analyzing diffraction patterns measured for different rotation angles of the sample, we determined the thickness of the crystals along this direction (see Fig. 2D and fig. S5). The thickness is quite homogeneous, and the histogram shows that most of the crystals have a thickness of 3.0 ± 0.1 μm with a root mean square (RMS) deviation of 0.7 ± 0.1 μm. This value is consistent with the observation in optical microscopy (~6 μm) that includes the surrounding ridges. Note that the thickness of the domains is significantly smaller than their lateral dimension (~10 μm; see Fig. 2A). The thickness of the crystallites and the appearance of only one hexagonal set of peaks at every position within the scale (see Fig. 2A and fig. S3) indicate that the photonic nanostructure is uniform in the direction perpendicular to the scale normal.

To achieve a more in-depth understanding of the structure of the photonic crystal at the nanoscale, we "zoomed in" on Fig. 2A using x-ray ptychography (*31*, *34*). A ptychographic reconstruction is presented in Fig. 3A (see also Materials and Methods and figs. S6 and S7). The hexagonal symmetry of the {111} planes can be clearly visualized, and the observed periodicity is in accordance with the expected unit cell size of 330 nm. The color in this figure represents the crystal orientation within the plane of the scale, determined as the azimuthal angle of the brightest peak in the Fourier transform of a masked region around each voxel. Ptychography allowed us not only to study the orientation of individual domains but also to visualize domain boundaries. Figure 3A reveals sharp domain boundaries with abrupt variation of lattice orientation, which are highlighted by the rapid color changes, for instance, between cyan and red or between cyan and yellow.

Additionally, we observed another type of domain boundary involving a more subtle angular variation, for instance, between red and dark red (see Fig. 3B; the white line highlights the domain boundary). These domain boundaries are accompanied by edge dislocations, which are more pronounced in the Bragg filtered image (see Fig. 3C) (*35*). We observed three edge dislocations, with two of the dislocations with a Burgers vector pointing to the left and one pointing to the right. Figure 3D shows a simulated diffraction pattern in the presence of edge dislocations and contains peaks with minimum intensity in the peak center, very similar to the recorded diffraction data shown in Fig. 1D. By counting the edge dislocations in Fig. 3A and comparing them with the total number of unit cells, we obtain a dislocation density of about 0.2%.

Figure 3E shows the phase of the complex transmission function determined in our experiment. The phase reveals ridges visible in the optical microscopy image of the scale (see Fig. 1C), even though these ridges are not clearly seen in the reconstructed modulus of the absorption function. The spacing of features in the phase image is about 1 μm, in agreement with the ridge spacing seen in the optical microscopy data. The phase oscillates with an amplitude of 0.3 ± 0.1 rad, and from the refractive index of chitin at an x-ray photon energy of 1.8 keV, we can estimate the relative density of the ridges (their height is about 3 μm because the total thickness of the scale is 6 μm and the photonic crystal is 3 μm thick) to be 7 ± 2%.

DISCUSSION

Our findings are consistent with the following growth model for these photonic nanostructures. The appearance of domains with random orientation of the gyroid lattice in the plane of the scale suggests that photonic crystals nucleate from multiple random locations. The preferred orientation of the domains, normal to the scale plane, is quite remarkable and is consistent with crystal nucleation at the scale boundary and crystal growth outward. The orientation could also arise from a secondary growth mechanism, in which domain orientations favored by surface energy grow at the expense of less-favored domain orientations (*36*). However, this rearrangement requires sufficient mobility, and both dislocations and rough domain boundaries, revealed by high-resolution x-ray data, suggest that the crystal structure is very rigid and is trapped in a nonequilibrium state (in particular, see the two edge dislocations with opposite Burgers vectors in Fig. 3A). The fact that we only observe one domain within the scale thickness further suggests that the domains grow from only one scale boundary.

The study of the nanoscale structure reveals two kinds of domain boundaries; first, we observe sharp interfaces with an abrupt change of the lattice orientation. We attribute these domain boundaries to the merging of domains independently nucleated during growth, that

terminate at the mutual domain boundary. The thickness of the interface between domains appears to be on the order of one unit cell, which is extremely sharp, considering that Fig. 3 shows a projection of about 10 layers (for example, see the region between cyan and red in Fig. 3B). Second, a different type of domain boundary appears between only slightly misaligned domains and is accommodated by a series of edge dislocations. These edge dislocations may form as a result of the merging of different domains with a low-angle tilt (*37*). However, edge dislocations with opposite Burgers vectors likely form as a result of the growth process itself and are introduced to mitigate internal stresses, possibly due to the curvature of the underlying scale or the plastic deformation during growth. A recent microscopic model of the growth of these crystals proposes an asymmetric triblock copolymer development (ABCB′A′) (*7*, *24*), and the out-of-equilibrium structures observed here indicate a rapid solvent evaporation, analogous to block copolymer structures trapped in a nonequilibrium state during solvent evaporation (*38*). The discovery of the edge dislocations in the biological photonic crystals is particularly remarkable because artificially manufactured topological defects in photonic crystals lead to interesting optical properties such as Anderson localization of light (*14*). Two intriguing questions are whether nature-engineered defects for a particular purpose and whether mimicking similar growth conditions allows for controlled manufacturing of defects in artificial photonic structures.

In summary, we have used x-ray diffraction to study domain morphology and domain boundaries within photonic crystals in a single butterfly wing scale. The photonic crystal is reminiscent of a thin polycrystalline film, with the domains being highly oriented in the direction normal to the scale boundary, which suggests a layer-by-layer crystal growth process starting at the cell membrane. Ptychographic imaging on the nanoscale has revealed two types of domain interfaces: abrupt boundaries likely due to the merging of independently nucleated domains and smooth interfaces with edge dislocations. We anticipate that the latter results from strain relaxation during crystal growth. Our study was performed nondestructively (nonslicing) and can, in principle, be extended to in vivo studies during the growth of these structures. Understanding and artificially reproducing these growth processes in the laboratory environment will be invaluable for developing future photonic devices. Finally, the multiple-Bragg-peak ptychography opens up high-resolution imaging of photonic crystals in the soft x-ray regime as well as of granular atomic crystals with coherent, high-energy x-rays (~100 keV) at the future diffraction-limited storage rings (*39*).

MATERIALS AND METHODS

Experimental details

The experiment was conducted at the 2-ID-B beamline at the Advanced Photon Source (*40*) by using angular resolved microdiffraction and a coherent x-ray diffraction technique called ptychography (see Fig. 1B) (*31*). We studied a single scale of the *T. imperialis* butterfly wing that was previously isolated and glued free-standing on a piece of kapton attached to a metal sample holder (see Fig. 1C for an optical micrograph). X-ray radiation from an undulator was used, and a photon energy of 1.8 keV was selected using a spherical grating monochromator. A pinhole 5 μm in diameter was positioned in front of the sample and both were placed in air between two evacuated tubes sealed by silicon nitride membranes. Helium gas flow was used to reduce air scattering and absorption. A charge-coupled device detector (CCD) with a pixel size of 22.5 × 22.5 μm^2 was positioned at a distance of about 0.5 m downstream from the sample. A region of interest 512 × 512 pixels in size was selected for our measurements, and in these conditions, the maximum momentum transfer corresponds to a resolution element of about 30 nm in the sample image. For microdiffraction scans presented in Fig. 2, 4 × 4 binning was used to reduce the readout time, and due to binning, no ptychography was possible.

Microdiffraction and orientation finding of the crystallites

We scanned the scale spatially for nine equidistant angles of incidence between −20° and +20°. The spatially resolved average intensities from all nine scans were cross-correlated, and an overlap was found. In this way, the set of spatially resolved measurements at different angles was transformed into a tomographic measurement at each position in the scale. At each spatial position, the observed Bragg peaks were identified, and the sample rotation angle θ and azimuthal angle ϕ of the Bragg peaks were found (the length, *Q*, of the scattering vector was fixed). The orientation determination procedure is presented graphically in figs. S1 and S2.

The width-finding procedure is depicted schematically in fig. S4. The thickness of the crystallographic grain along the x-ray beam can be determined by the width of the peaks in θ, which was found by fitting a Gaussian $\exp[-(\theta/c)^2]$ to the horizontal line scans in figs. S1B and S2B. The thickness was found using equation

$$d_z = \frac{d_0}{2|\sin(\phi)|c}$$

where d_0 is 330 nm and c is the width of the Gaussian fit. The approximation $\tan(\theta) = \theta$ was used ($\theta < 20°$), and the factor of 2 accounts for the difference between the full width at half maximum of a Gaussian fit and $[\sin(q_z d_z/2)/(q_z d_z/2)]^2$, which describes the diffracted intensity of a slab of thickness d_z along the q_z direction (see Fig. 1).

Ptychographic reconstructions

We collected a raster scan of 6 × 6 diffraction patterns (similar to Fig. 1, D and E) from illumination areas separated by 1.5 μm in both directions and exposed for 25 s with a maximum of 1.6×10^4 photons per pixel. The data were reconstructed using an alternation of difference map and ePIE algorithms (*31*) and a total of 1260 iterations. A Gaussian mask was used to suppress the high *Q* data in the beginning of the reconstruction and was subsequently extended to include high *Q* data to the end of the reconstruction. The code was modified for graphic processing unit acceleration, and 200 independent reconstructions each with a different random starting guess were made. The initial guess for the probe function was obtained from measurements of a test sample.

The high-crystallinity region of the data (red region in Fig. 3; 201 × 201 pixels) for all 200 reconstructions was cross-correlated, and the pattern with the highest number of similar patterns was selected. Presented in the text is the average of 25 complex reconstructed images, which have a high correlation coefficient with the selected pattern. Different reconstructions were slightly shifted with respect to each other, and the overlap between different images was adjusted

by a cross-correlation analysis before averaging. The final amplitude and phase from the reconstruction are shown in fig. S6.

The reconstruction results could be slightly affected by the sample-detector distance (*41*, *42*). In our experiment, the sample-detector distance was somewhat uncertain and different sets of reconstructions corresponding to various sample-detector distances were conducted. The number of voxels representing the pinhole shift of 1.5 μm during the ptychographic scan was used to define this distance. The size of a voxel, D, in the real space was found to be between D = 1.5 μm/52 = 28.8 nm and D = 30 nm (see fig. S7A). The main features of the reconstruction (domain boundaries and edge dislocations) do not depend strongly on the real-space voxel size. Reconstructions performed with D = 30 nm and D = 28.8 nm produced visually indistinguishable patterns (see fig. S7, B and C), and the reconstruction with D = 28.8 nm is shown in the text.

SUPPLEMENTARY MATERIALS

Supplementary material for this article is available at http://advances.sciencemag.org/cgi/content/full/2/6/e1600149/DC1

fig. S1. Orientation determination procedure for one grain.
fig. S2. Orientation determination procedure for multiple grains.
fig. S3. Description of angles used in the microdiffraction analysis.
fig. S4. Distribution of grain orientations.
fig. S5. A sketch describing the procedure determining the width of the crystal.
fig. S6. Amplitude (absorption) and phase of the ptychographic reconstruction.
fig. S7. Robustness of the ptychographic reconstruction.

REFERENCES AND NOTES

1. L. Rayleigh, VII. On the optical character of some brilliant animal colours. *Philos. Mag. Ser. 6* **37**, 98–111 (1919).
2. A. R. Parker, R. C. McPhedran, D. R. McKenzie, L. C. Botten, N. A. Nicorovici, Photonic engineering. Aphrodite's iridescence. *Nature* **409**, 36–37 (2001).
3. P. Vukusic, J. R. Sambles, C. R. Lawrence, R. J. Wootton, Quantified interference and diffraction in single Morpho butterfly scales. *Proc. R. Soc. London Ser. B* **266**, 1403–1411 (1999).
4. P. Vukusic, R. Sambles, C. Lawrence, G. Wakely, Sculpted-multilayer optical effects in two species of *Papilio* butterfly. *Appl. Opt.* **40**, 1116–1125 (2001).
5. P. Vukusic, J. R. Sambles, Review article photonic structures in biology. *Nature* **424**, 852–855 (2003).
6. A. L. Ingram, A. R. Parker, A review of the diversity and evolution of photonic structures in butterflies, incorporating the work of John Huxley (The Natural History Museum, London from 1961 to 1990). *Philos. Trans. R. Soc. London Ser. B* **363**, 2465–2480 (2008).
7. V. Saranathan, C. O. Osuji, S. G. J. Mochrie, H. Noh, S. Narayanan, A. Sandy, E. R. Dufresne, R. O. Prum, Structure, function, and self-assembly of single network gyroid ($I4_132$) photonic crystals in butterfly wing scales. *Proc. Natl. Acad. Sci. U.S.A.* **107**, 11676–11681 (2010).
8. B. D. Wilts, K. Michielsen, H. De Raedt, D. G. Stavenga, Iridescence and spectral filtering of the gyroid-type photonic crystals in *Parides sesostris* wing scales. *Interface Focus* **2**, 681–687 (2012).
9. B. D. Wilts, K. Michielsen, H. De Raedt, D. G. Stavenga, Sparkling feather reflections of a bird-of-paradise explained by finite-difference time-domain modeling. *Proc. Natl. Acad. Sci. U.S.A.* **111**, 4363–4368 (2014).
10. J. Teyssier, S. V. Saenko, D. van der Marel, M. C. Milinkovitch, Photonic crystals cause active colour change in chameleons. *Nat. Commun.* **6**, 6368 (2015).
11. T. M. Jordan, J. C. Partridge, N. W. Roberts, Non-polarizing broadband multilayer reflectors in fish. *Nat. Photonics* **6**, 759–763 (2012).
12. T. M. Jordan, J. C. Partridge, N. W. Roberts, Disordered animal multilayer reflectors and the localization of light. *J. R. Soc. Interface* **11**, 20140948 (2014).
13. R. D. Reed, R. Papa, A. Martin, H. M. Hines, B. A. Counterman, C. Pardo-Diaz, C. D. Jiggins, N. L. Chamberlain, M. R. Kronforst, R. Chen, G. Halder, H. F. Nijhout, W. O. McMillan, *optix* drives the repeated convergent evolution of butterfly wing pattern mimicry. *Science* **333**, 1137–1141 (2011).
14. O. Painter, J. Vučković, A. Scherer, Defect modes of a two-dimensional photonic crystal in an optically thin dielectric slab. *J. Opt. Soc. Am. B* **16**, 275–285 (1999).
15. T. Schwartz, G. Bartal, S. Fishman, M. Segev, Transport and Anderson localization in disordered two-dimensional photonic lattices. *Nature* **446**, 52–55 (2007).
16. R. A. Potyrailo, H. Ghiradella, A. Vertiatchikh, K. Dovidenko, J. R. Cournoyer, E. Olson, *Morpho* butterfly wing scales demonstrate highly selective vapour response. *Nat. Photonics* **1**, 123–128 (2007).
17. L. Sapienza, H. Thyrrestrup, S. Stobbe, P. D. Garcia, S. Smolka, P. Lodahl, Cavity quantum electrodynamics with Anderson-localized modes. *Science* **327**, 1352–1355 (2010).
18. M. Saba, M. Thiel, M. D. Turner, S. T. Hyde, M. Gu, K. Grosse-Brauckmann, D. N. Neshev, K. Mecke, G. E. Schröder-Turk, Circular dichroism in biological photonic crystals and cubic chiral nets. *Phys. Rev. Lett.* **106**, 103902 (2011).
19. L. Lu, L. Fu, J. D. Joannopoulos, M. Soljačić, Weyl points and line nodes in gyroid photonic crystals. *Nat. Photonics* **7**, 294–299 (2013).
20. J. Huang, X. Wang, Z. L. Wang, Controlled replication of butterfly wings for achieving tunable photonic properties. *Nano Lett.* **6**, 2325–2331 (2006).
21. C. Mille, E. C. Tyrode, R. W. Corkery, 3D titania photonic crystals replicated from gyroid structures in butterfly wing scales: Approaching full band gaps at visible wavelengths. *RSC Adv.* **3**, 3109–3117 (2013).
22. A. Argyros, S. Manos, M. C. J. Large, D. R. McKenzie, G. C. Cox, D. M. Dwarte, Electron tomography and computer visualisation of a three-dimensional 'photonic' crystal in a butterfly wing-scale. *Micron* **33**, 483–487 (2002).
23. G. E. Schröder-Turk, S. Wickham, H. Averdunk, F. Brink, J. D. Fitz Gerald, L. Poladian, M. C. J. Large, S. T. Hyde, The chiral structure of porous chitin within the wing-scales of *Callophrys rubi*. *J. Struct. Biol.* **174**, 290–295 (2011).
24. V. Saranathan, A. E. Seago, A. Sandy, S. Narayanan, S. G. J. Mochrie, E. R. Dufresne, H. Cao, C. O. Osuji, R. O. Prum, Structural diversity of arthropod biophotonic nanostructures spans amphiphilic phase-space. *Nano Lett.* **15**, 3735–3742 (2015).
25. S. Yoshioka, H. Fujita, S. Kinoshita, B. Matsuhana, Alignment of crystal orientations of the multi-domain photonic crystals in *Parides sesostris* wing scales. *J. R. Soc. Interface* **11**, 20131029 (2014).
26. H. Ghiradella, Structure of butterfly scales: Patterning in an insect cuticle. *Microsc. Res. Tech.* **27**, 429–438 (1994).
27. H. Ghiradella, W. Radigan, Development of butterfly scales. II. Struts, lattices and surface tension. *J. Morphol.* **150**, 279–297 (1976).
28. V. L. Welch, J.-P. Vigneron, Beyond butterflies—The diversity of biological photonic crystals. *Opt. Quantum Electron.* **39**, 295–303 (2007).
29. C. Kumar, *Biomimetic and Bioinspired Nanomaterials* (John Wiley & Sons, Weiniheim, 2010).
30. K. Michielsen, D. G. Stavenga, Gyroid cuticular structures in butterfly wing scales: Biological photonic crystals. *J. R. Soc. Interface* **5**, 85–94 (2008).
31. P. Thibault, M. Dierolf, A. Menzel, O. Bunk, C. David, F. Pfeiffer, High-resolution scanning x-ray diffraction microscopy. *Science* **321**, 379–382 (2008).
32. J. V. I. Timonen, M. Latikka, L. Leibler, R. H. A. Ras, O. Ikkala, Switchable static and dynamic self-assembly of magnetic droplets on superhydrophobic surfaces. *Science* **341**, 253–257 (2013).
33. J. Gulden, O. M. Yefanov, A. P. Mancuso, V. V. Abramova, J. Hilhorst, D. Byelov, I. Snigireva, A. Snigirev, A. V. Petukhov, I. A. Vartanyants, Coherent x-ray imaging of defects in colloidal crystals. *Phys. Rev. B* **81**, 224105 (2010).
34. J. M. Rodenburg, A. C. Hurst, A. G. Cullis, B. R. Dobson, F. Pfeiffer, O. Bunk, C. David, K. Jefimovs, I. Johnson, Hard-x-ray lensless imaging of extended objects. *Phys. Rev. Lett.* **98**, 34801 (2007).
35. M. J. Hÿtch, E. Snoeck, R. Kilaas, Quantitative measurement of displacement and strain fields from HREM micrographs. *Ultramicroscopy* **74**, 131–146 (1998).
36. C. V. Thompson, Grain growth in thin films. *Annu. Rev. Mater. Sci.* **20**, 245–268 (1990).
37. N. W. Ashcroft, N. D. Mermin, *Solid State Physics* (Holt, Rinehart and Winston, Orlando, ed. 1, 1976).
38. R. A. Segalman, Patterning with block copolymer thin films. *Mater. Sci. Eng. R* **48**, 191–226 (2005).
39. M. Eriksson, J. F. van der Veen, C. Quitmann, Diffraction-limited storage rings — A window to the science of tomorrow. *J. Synchrotron Radiat.* **21**, 837–842 (2014).
40. I. McNulty, A. M. Khounsary, Y. P. Feng, Y. Qian, J. Barraza, C. Benson, D. Shu, A beamline for 1-4 keV microscopy and coherence experiments at the Advanced Photon Source. *Rev. Sci. Instrum.* **67**, 3372 (1996).
41. H. Burdet, G. R. Morrison, X. Huang, X. Shi, J. N. Clark, F. Zhang, M. Civita, R. Harder, I. K. Robinson, Observations of artefacts in the x-ray ptychography method. *Opt. Express* **22**, 10294–10303 (2014).
42. M. Rose, P. Skopintsev, D. Dzhigaev, O. Gorobtsov, T. Senkbeil, A. von Gundlach, T. Gorniak, A. Shabalin, J. Viefhaus, A. Rosenhahn, I. Vartanyants, Water window ptychographic imaging with characterized coherent X-rays. *J. Synchrotron Radiat.* **22**, 819–827 (2015).
43. Anagoria: Museum für Naturkunde Berlin (used under CC-BY); https://commons.wikimedia.org/wiki/File:2013_Naturkunde-Museum_Berlin_teinopalpus_imperialis_anagoria.JPG (viewed by May 30, 2016).

Acknowledgments: We acknowledge Y. Nashed and A. Tripathi for sharing their code for ptychographic reconstructions, N. Hua for careful reading of the manuscript, and M. Goldflam and D. Basov for the use of the optical microscope. We also thank R. Harder for assistance during

the measurements. **Funding:** This work at the University of California, San Diego, was supported by the U.S. Department of Energy (DOE), Office of Science, Office of Basic Energy Sciences, under contract DE-SC0001805. S.G.J.M. was supported by the DOE, Office of Basic Energy Sciences under contract DE-SC0004162. Work at the Center for Nanoscale Materials and at the Advanced Photon Source was supported by the DOE, Office of Science, Office of Basic Energy Sciences, under contract DE-AC02-06CH11357. CXDI Algorithm Development was supported by DARPA PULSE Award 1550663. **Author contributions:** A.S., S.G.J.M., and O.G.S. designed the research. A.S., L.B., S.H.B., D.V., I.M., S.G.J.M., and O.G.S. performed the experiment. A.S. analyzed the data. A.S., K.E.J., E.R.D., R.O.P., S.G.J.M., and O.G.S. interpreted the results. A.S. wrote the manuscript with input from all authors. **Competing interests:** The authors declare that they have no competing interests. **Data and materials availability:** All data needed to evaluate the conclusions in the paper are present in the paper and/or the Supplementary Materials. Additional data related to this paper are available upon request to ansinger@ucsd.edu.

Submitted 26 January 2016
Accepted 19 May 2016
Published 10 June 2016
10.1126/sciadv.1600149

Citation: A. Singer, L. Boucheron, S. H. Dietze, K. E. Jensen, D. Vine, I. McNulty, E. R. Dufresne, R. O. Prum, S. G. J. Mochrie, O. G. Shpyrko, Domain morphology, boundaries, and topological defects in biophotonic gyroid nanostructures of butterfly wing scales. *Sci. Adv.* **2**, e1600149 (2016).

Domain morphology, boundaries, and topological defects in biophotonic gyroid nanostructures of butterfly wing scales

Andrej Singer, Leandra Boucheron, Sebastian H. Dietze, Katharine E. Jensen, David Vine, Ian McNulty, Eric R. Dufresne, Richard O. Prum, Simon G. J. Mochrie and Oleg G. Shpyrko

Sci Adv **2** (6), e1600149.
DOI: 10.1126/sciadv.1600149